Journal of Materials Chemistry A

Tailored Sustainable Synthesis of MoxC by Electrochemical Etching of Mo2TiAlC2 MAX Phase toward Electrochemical Application

Journal:	*Journal of Materials Chemistry A*
Manuscript ID	TA-ART-03-2025-001828.R1
Article Type:	Paper
Date Submitted by the Author:	15-Apr-2025
Complete List of Authors:	Sheng, Minhao; Xi'an Jiaotong University Bin, Xiaoqing; Xi'an Jiaotong University Que, Wenxiu; Xi'an Jiaotong University Asakura, Yusuke; Nagoya University, Department of Materials Process Engineering Yamauchi, Yusuke; University of Queensland, Chemical Engineering; Nagoya University,

Tailored Sustainable Synthesis of Mo_xC by Electrochemical Etching of Mo_2TiAlC_2 MAX Phase toward Electrochemical Application

Minhao Sheng [a], Xiaoqing Bin [a], Wenxiu Que [a, *], Yusuke Asakura [b, *], Yusuke Yamauchi [b, c, d, *]

[a] Electronic Materials Research Laboratory, Key Laboratory of the Ministry of Education & International Center for Dielectric Research, Shaanxi Engineering Research Center of Advanced Energy Materials and Devices, School of Electronic Science and Engineering, Xi'an Jiaotong University, Xi'an 710049, P. R. China.

[b] Department of Materials Process Engineering, Graduate School of Engineering, Nagoya University, Nagoya 464-8603, Japan;

[c] Australian Institute for Bioengineering and Nanotechnology (AIBN), The University of Queensland, Brisbane, Queensland 4072, Australia

[d] Department of Chemical and Biomolecular Engineering, Yonsei University, Seoul 03722, South Korea.

* wxque@mail.xjtu.edu.cn; asa.y@nagoya-u.jp; y.yamauchi@uq.edu.au

Abstract

Molybdenum carbide stands out as a promising material for energy-related applications, particularly as a hydrogen evolution reaction (HER) catalyst and a supercapacitor electrode material. However, traditional synthesis methods for molybdenum carbide are often complex, requiring multi-steps or severe conditions, which result in limited material accessibility and scalability. Herein, the work proposes a novel method for preparing molybdenum carbide materials with excellent HER catalytic performance and efficient SC capabilities by electrochemically etching the quaternary carbide (Mo_2TiAlC_2 MAX) precursor. The etching mechanism from Mo_2TiAlC_2 MAX to Mo_xC is systematically investigated by the experiment and the density functional theory (DFT) method. The results show that Ti and Al atoms can be completely removed by electrochemical etching in an alkaline K_2S solution. The resulting molybdenum carbide (Mo_xC) nanosheets exhibits remarkable HER catalytic activity due to its abundant metal vacancy defect structure. Especially, the Mo_xC delivers improved overpotentials (157 mV at 10 mA cm^{-2}) in 0.5 M H_2SO_4 compared to Mo_2TiAlC_2. Theoretical calculations unraveled that Mo_xC exhibited a reduced Gibbs free energy for the HER. The Mo_xC demonstrates as an optimal candidate for supercapacitor (SC) applications, exhibiting a high specific capacitance of 394 F g^{-1} at 2 mV s^{-1} and excellent cycling stability, retaining nearly 94.7% of its initial capacity after 5000 cycles. The as-fabricated asymmetric supercapacitor exhibits maximum energy density of 12.4 Wh kg^{-1} at a power density of 89.1 W kg^{-1} and the capacity retention rate can still up to 80.2% even after 6000 cycles at a current density of 1 A g^{-1}.

Keywords: electrochemical etching, molybdenum carbide, electrocatalyst, hydrogen evolution reaction, supercapacitor.

1. Introduction

To address the dual challenges of energy scarcity and escalating environmental degradation, the scientific community is increasingly focusing on hydrogen as a viable alternative to conventional fossil fuels. The electrochemical hydrogen evolution reaction (HER) is a key pathway for the efficient production of hydrogen.[1] The primary challenge in this field lies in developing catalysts that combine high efficiency with economic viability. The optimization of catalyst activity, stability, and cost-effectiveness is essential for advancing the hydrogen application, especially in water electrolysis driven by renewable energy sources. Meanwhile, there has been a surge of interest in high-power-density supercapacitors (SC), driven by the growing demand for energy storage systems capable of delivering rapid charge–discharge rates. The exploration of materials capable of simultaneously achieving efficient HER and SC performance is recognized as a significant challenge. Dual-function materials require a delicate balance between catalytic activity potentials and energy storage windows.[2] The development of such materials often involves complex design strategies, including optimizing their electronic structures, engineering surface-active sites, and integrating multifunctional properties.

Transition metal carbides have emerged as exceptional candidates for the HER and SC performance due to their affordability, metallic conductivity, mechanical robustness, and outstanding catalytic efficiency.[3-8] Among these, molybdenum-based carbides (Mo_xC) have gained attention for their unique surface electronic properties and high chemical stability. The most common synthesis methods for molybdenum carbides are high-temperature carbothermal reduction and chemical vapor deposition (CVD), both of which are bottom-up approaches.[9, 10] However, these methods often result in the formation of a carbon layer on the surface of the Mo_xC. Researchers have verified that the carbon layer on the surface of molybdenum carbide synthesized by CVD was proved to inhibit the catalytic activity.[11, 12] Another top-down approaches, such as chemical etching, has also been successful in obtaining Mo_2C MXene. For example, Halim achieved the synthesis of Mo_2C by etching gallium from the ternary transition metal carbide Mo_2Ga_2C.[13] Unfortunately, the etching process requires the use of hazardous and high-concentration HF acid solutions,[14-17] which pose significant risks. To address these challenges,

researchers are exploring safer and more environmentally friendly methods for the synthesis. In fact, green and safe electrochemical synthesis techniques have already been used to produce micro/nanostructured metal carbides (Ti_3C_2 or V_2C) *via* anodic etching of MAX (Ti_3AlC_2, V_2AlC) phases.[18, 19] Moreover, Pang et. al. proposed an electrochemical etching method for Mo_2TiAlC_2 or Mo_2GaC_2 in a diluted HCl electrolyte at a mild heating temperature of 55°C and a small applied potential of 0.7 V vs. RHE, resulting in the removal of the aluminum or gallium layer from the MAX phase to obtain the corresponding molybdenum-based carbides.[20] Therefore, this approach leverages the excellent electrical conductivity of MAX to selectively etch non-molybdenum metals, exploiting the different oxidation potentials of the constituent metal elements to form Mo_xC.

In the early stages of our research, we selected the conductive double-transition metal Mo_2TiAlC_2 MAX as the etching precursor.[21] Using an electrochemical system with a suitable electrolyte, we aimed to selectively etch out the metallic elements Al and Ti. However, this process initially proved incomplete, resulting in a significant amount of unreacted Mo_2TiAlC_2 in the etched product.[21] In this study, two-dimensional molybdenum carbide (Mo_xC) nanosheets are prepared by electrochemical etching of Mo_2TiAlC_2 in a two-electrode system at room temperature. We choose alkaline potassium sulfide (K_2S) solution as the etching medium, and our results confirm that this mildly alkaline K_2S solution selectively removed Al and Ti atoms from Mo_2TiAlC_2, yielding an Mo_xC structure. Instead of the traditional approach of electrochemical stripping two-dimensional materials and then collecting the products from the electrolyte, we innovatively choose a three-dimensional conductive skeleton carbon cloth (CC) as a negative collector for direct electrodeposition to form Mo_xC@CC. During the continuous process of anodic electrochemical etching, ultrathin Mo_xC nanoplates in the electrolyte are directly electrodeposited onto the cathode. In this step, the anodic etching reaction and the cathodic deposition reaction occur simultaneously, achieving the safe and efficient sustainable formation of Mo_xC as well as the rapid separation of Mo_xC products from the electrolyte solution. Within just a few minutes, we obtain the final Mo_xC@CC electrode directly from Mo_2TiAlC_2, avoiding the need for subsequent cleaning and

eliminating the wastewater generally generated by conventional etching methods. Here, the phase composition of the products prepared under different etching conditions is analyzed, and the formation process of Mo_xC is discussed. Also, the performances of Mo_xC@CC as an electrochemical hydrogen evolution catalyst and a SC electrode material are studied as a proof of concept.

2. Results and Discussion

Figure 1 presents a schematic illustration of the electrolytic setup, along with the atom structure of Mo_2TiAlC_2 and the theoretical Mo_xC structure after the etching process. The electrochemical etching of Mo_2TiAlC_2 was conducted in a simple two-electrode system (for detailed implementation, referring to the experimental section). An aqueous potassium sulfide solution was selected as the etching medium due to its cost-effectiveness and moderately strong alkaline properties. It is confirmed that varying OH^- ion concentrations in aqueous solutions affects the etching efficiency of metal elements in Mo_2TiAlC_2: low OH^- concentrations slow the etching process, while overly high concentrations leave behind only the carbon framework.[21-23] The pH value of potassium sulfide solutions with various mass fractions is approximately 11.5 (0.025 g mL^{-1}: 11.29, 0.05 g mL^{-1}: 11.55, 0.075 g mL^{-1}: 11.79). In this paper, an etching solution concentration of 0.05 g mL^{-1} was used. Typical cyclic voltammograms (Figure S1) revealed three distinct states at the anode, corresponding to different reactions (Stage I: non-Faradaic double-layer reaction, evident as a CV plateau from 0-2 V; Stage II: water splitting reaction from 2-3 V, marked by an initial rise in current; Stage III: dealloying of ceramic Mo_2TiAlC_2, characterized by a sharp current increase beyond 3 V).

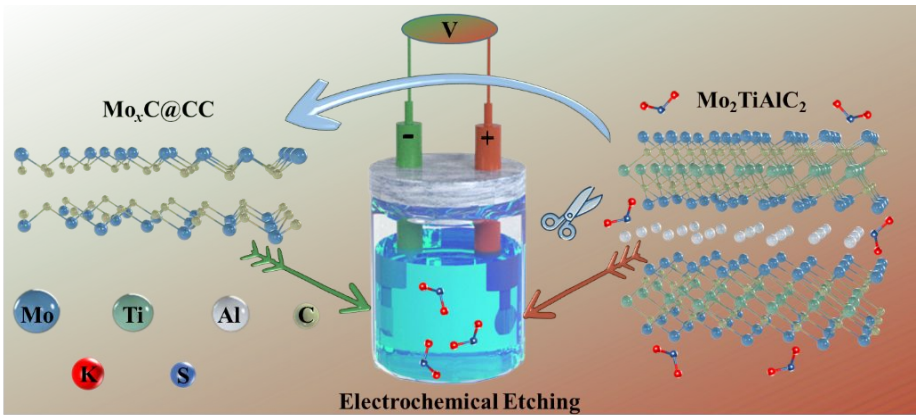

Figure 1. Schematic diagram of electrochemical etching of Mo_2TiAlC_2 for formation of Mo_xC@CC on two-electrode cell. Mo_2TiAlC_2 and CC are set on anode and cathode, respectively.

To verify the successful synthesis of Mo_xC due to corrosion of Ti and Al metal elements from Mo_2TiAlC_2 under electrochemical etching, we analyzed the composition of the product after reaching a potential of 3 V. X-ray diffraction (XRD) analysis (Figure 2a) of the precursor showed sharp and well-defined peaks at angles of 9.72°, 19.22°, 28.94°, 35.12°, and 39.96° corresponding specifically to the (002), (004), (006), (101), and (104) planes of Mo_2TiAlC_2 structure, indicating a highly pure phase with no impurities. The localized smooth surface (Figure S2) and the densely laminated structure confirm the successful formation of Mo_2TiAlC_2. After applying a voltage of 3 V for one hour, the K_2S solution turned noticeably cloudy, a uniform and deep black Mo_xC sediment formed on the surface of the cathode carbon cloth (Figure S3a-c). The black Mo_xC material adhered strongly to the carbon cloth and cannot be removed by simple rinsing. The stable deposition of Mo_xC on the carbon cloth (Mo_xC@CC) offers potential for its direct use as a catalyst electrode. The XRD patten of Mo_xC@CC shows two broad diffraction peaks at around 26° and 43° attributed to the carbon cloth (Figure 2a). To better characterize the crystal structure of Mo_xC, Mo_xC powder was collected from the carbon cloth substrate using ultrasonic treatment. The Mo_xC powder exhibits a broad peak in the 20-30° range, indicating amorphous phase or polycrystallized phase. The absence of residual peaks corresponding to the parent Mo_2TiAlC_2 structure conformed the

thoroughness of the etching process.

To further investigate the etching mechanism, we analyzed the composition of the electrolytic solution. During the electrochemical etching, Mo_xC detached from the Mo_2TiAlC_2 anode mixed with elemental sulfur produced by a side reaction at the anode (S^{2-}-$2e^-\rightarrow S$) in the electrolyte. Without washing with a hot 1 M KOH solution, the collected solution appeared yellow after several rounds of centrifugation with ultrapure water (Figure S3d), indicating the presence of S_8. By vacuum filtration, the XRD pattern of the collected powder (Figure S4a) matches that of S_8 (PDF#74-1465), and S_8 diffraction peaks obscures the amorphous Mo_xC signal. To remove the S_8 impurity, the hot KOH solution was used to dissolve the S_8 powder, resulting in a clean Mo_xC product consistent with the cathode deposition, as verified by XRD patterns (Figure S4b).

Raman spectroscopy (Figure 2b) was employed to further characterize the carbon-based Mo_xC materials, showing two pronounced peaks at 1330 cm^{-1} and 1600 cm^{-1}, corresponding to the disordered (D) band and graphite (G) band, respectively, at etching voltages of 3-5 V. The I_D/I_G intensity ratio, an indicator of carbon disorder, increases with etching voltage, rising from 1.09 at 3 V to 1.20 at 4 V, and reaching 1.23 at 5 V,[24-26] indicating more defective structures at higher potential. This suggests that the applied anode voltage not only oxidizes and etches Mo_2TiAlC_2 but also facilitates electrophoretic deposition of etching products onto the cathode. Scanning electron microscopy (SEM) analysis was conducted to confirm the morphology of Mo_xC. Uniform flat Mo_xC nanosheets are directly deposited on the surface of the carbon cloth surface (Figure 2c). The nanosheets are tightly stacked and assembled onto the surface of carbon cloth under the influence of an electric field. The bulk flake morphology of Mo_xC powder collected from the solution after hot KOH solution cleaning shows a similar structure (Figure 2d). For enhanced visual contrast, using a metal aluminum foil cathode instead of carbon cloth produced a clearer black-and-white contrast as shown in the SEM image (Figure S5), demonstrating uniform Mo_xC nanosheet deposition. These observations suggest that the cathode primarily acts as a deposition substrate without directly participating in the electrochemical reaction.

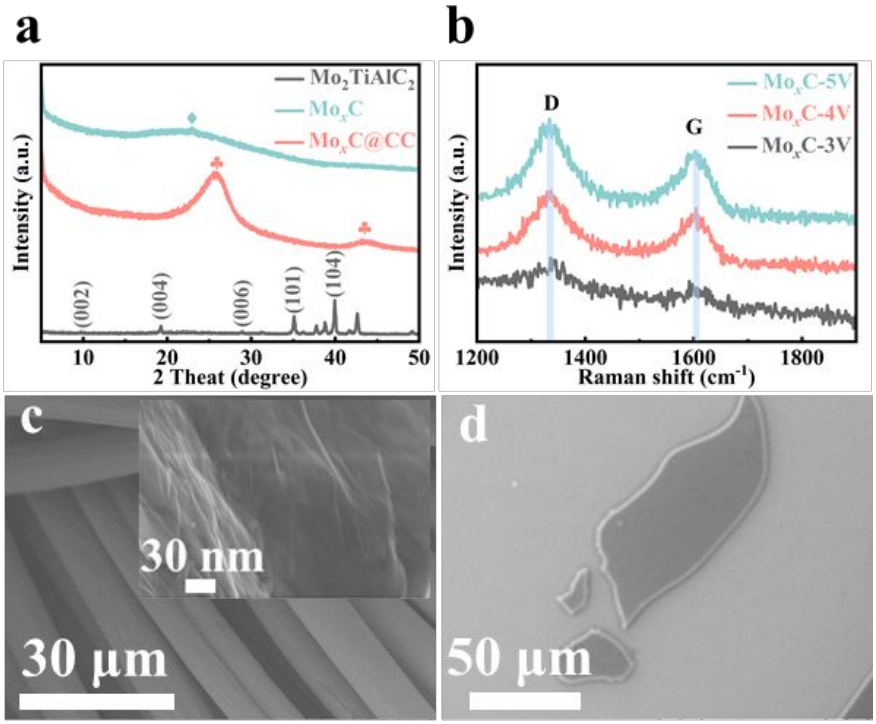

Figure 2. (a) XRD patterns of Mo_2TiAlC_2, Mo_xC, and Mo_xC@CC etched at 3 V. (b) Raman spectra of Mo_xC@CC at different etching voltages. SEM image of (c) Mo_xC@CC (The inset shows nanosheets exfoliated from carbon cloth by sonication in ethanol solution) and (d) Mo_xC powder on Si wafer after hot KOH solution cleaning at 3 V.

Transmission electron microscopy (TEM) and high-resolution TEM images further demonstrates that the thick Mo_2TiAlC_2 is etched and transformed into thin Mo_xC nanosheets by electrochemical etching. The Mo_xC nanosheets are peeled from the carbon cloth by adding alcohol and then intense ultrasound. The Mo_xC etched at 3 V has numerous micropores (Figure 3a, b), which facilitates the rapid accumulation and transport of H^+ ions, enhancing electrochemical properties. For some regions of the sample (Figure S6), no obvious crystal diffraction spot is observed in the Fourier transform (FFT) pattern from the TEM image, only the diffused halo. And the FFT image of the other region (Figure 3c) confirms the presence of reflections corresponding to a hexagonal crystal structure, indicating the crystallized MoC.[27] The observed lattice fringes with a spacing of 0.226 nm correspond to the (104) plane of MoC.[4] Therefore, both amorphous and polycrystalline phases of Mo_xC coexist in

the sample. Additionally, abundant Mo vacancy defects are visible, suggesting that partial Mo atoms in Mo_2TiAlC_2 were electrochemically etched in the potassium sulfide solution. To further verify the existence of Mo vacancies, electron paramagnetic resonance (EPR) was performed, as shown in Figure 3d. No obvious signal is detected for Mo_2TiAlC_2, demonstrating its good crystalline property with negligible defects before etching. As to Mo_xC, the broad signal should be ascribed to the Mo^{5+} species, which further confirms the successful construction of Mo vacancy defects[28] Element mapping reveals that Mo, C, O, and S elements are uniformly distributed on the Mo_xC surface, while Ti and Al signals are nearly absent (Figure 3e). This observation confirms that most Ti and Al atoms were etched away, resulting in Mo_xC-dominant structure on the exterior of Mo_2TiAlC_2. The Zeta potential results (Figure S7) shows that the surface of Mo_xC is negatively charged, which is speculated to be mainly due to the -O groups introduced during the electrochemical etching process. The presence of numerous -O functional groups in the Mo_xC deposited on the cathode can positively impact electrochemical hydrogen evolution performance.[29, 30] To more accurately determine the metal element proportions in Mo_xC , ICP tests (Table S1) were performed on the Mo, Ti, and Al elements in both Mo_2TiAlC_2 and Mo_xC at different etching voltages to clarify the migration pattern of these elements. After the completion of electrolysis, the Ti and Al contents of Mo_xC@CC decreased by nearly a hundredfold, confirming complete removal of Ti and Al atoms. As the etching voltage increases, the Mo concentration proportionally decreased, indicating that partial Mo atoms were also etched away. Therefore, it is difficult to detect the diffraction peak of molybdenum carbide in XRD and the obvious long-range ordered structure in TEM.

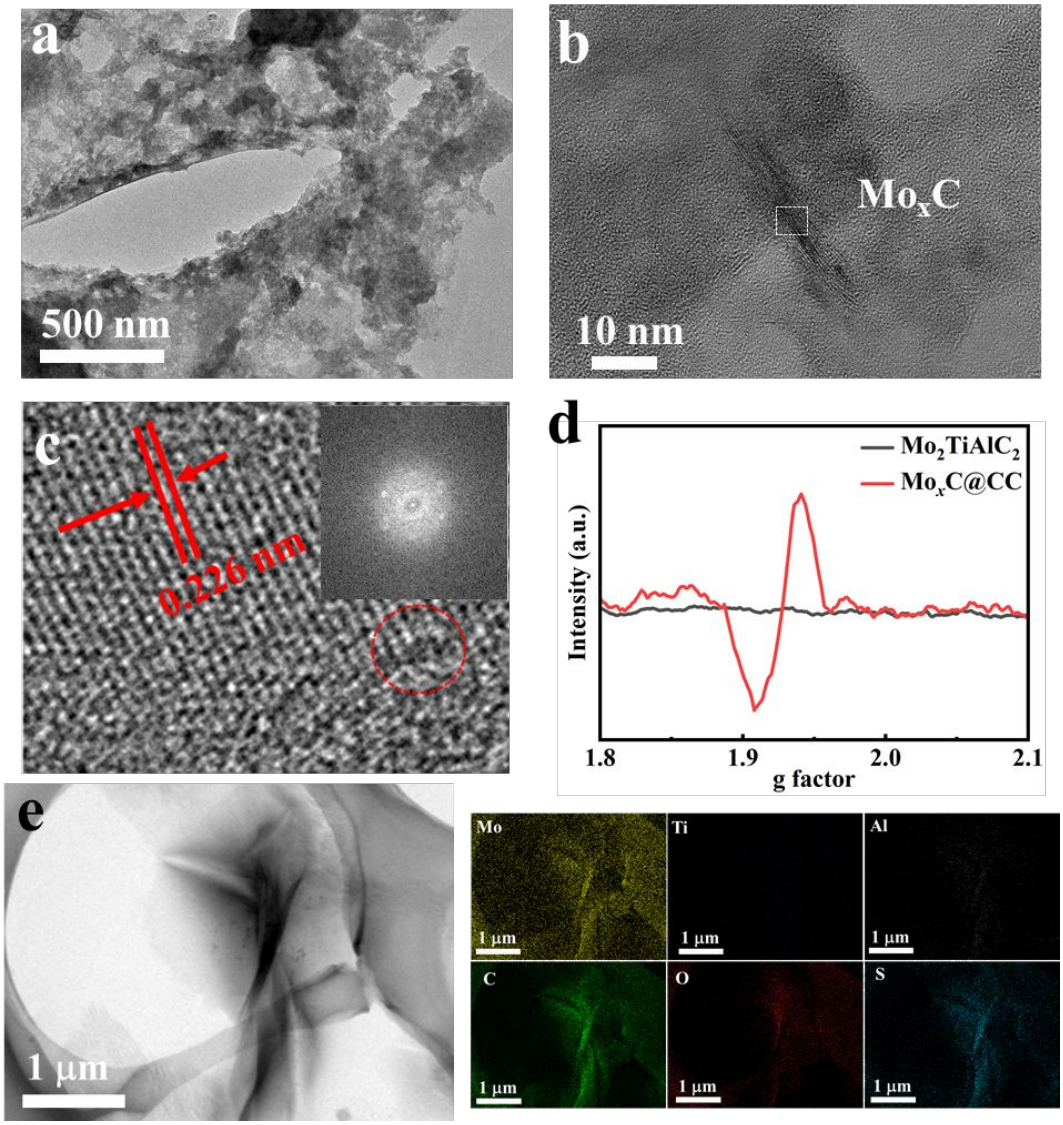

Figure 3. (a) TEM of Mo_xC@CC etched at 3 V. (b) HRTEM of Mo_xC@CC etched at 3 V. (c) HRTEM area enlargement of Mo_xC@CC. (Inset: the corresponding FFT patterns of parts). (d) EPR spectra of Mo_2TiAlC_2 and Mo_xC@CC. (e) STEM image of Mo_xC@CC and corresponding EDX mapping images.

To gain a deeper understanding of the electrochemical etching mechanism, density functional theory (DFT) calculations were performed to evaluate the stability of the etching products. Based on formation energy analysis, the complete removal of Al and Ti atoms results in the transformation of Mo_2TiAlC_2 to MoC, with a formation energy of 0.85 eV/atom (Figure 4a). Conventional acid etching has successfully removed the Al atoms from Mo_2TiAlC_2, yielding Mo_2TiC_2 MXene.[14, 31, 32] Compared to the more reactive metallic Mo-Al bonds, the Ti-C covalent bonds in Mo_2TiAlC_2 make the etching process

more challenging, requiring additional energy input to drive the conversion. Thus, electrochemical etching is essential to facilitate this reaction. The high surface energy of Mo_xC makes it highly susceptible to modification by surface functional groups (e.g., -O), enhancing its effectiveness as active electrode materials. In order to further reveal the atomic etching effect of the etching medium on Mo_2TiAlC_2, the electron localization function (ELF) was simulated by DFT, where ELF = 1 corresponds to the perfect localization, ELF = 0.5 indicates the electron gas, and ELF = 0 refers to complete delocalization.[33-35] As shown in Figure 4b, the Al atom is located between two adjacent layers of Mo atoms in the original Mo_2TiAlC_2. The etching process is simulated by fixing the atoms in the shaded area on the left edge and increasing the amount of OH^- and S^{2-} at the open boundary of Mo_2TiAlC_2. The atomic configuration with the lowest energy of ELF obtained by etching Mo_2TiAlC_2 is shown in Figure 4b-f. It can be clearly seen that the Al atom on the right edge forms an Al-O bond with the foreign O atom (from OH^-), thereby moving outward, indicating that Al is successfully dissociated from the Mo_2TiAlC_2 host. In addition, the S^{2-} ions can move outward with the Ti atom, indicating that the S ions can coordinate with Ti and achieve the dissociation of Ti. With the increase in the amount of S^{2-} and OH^- added, the interaction between Al and the surrounding Mo atoms weakens, and the Ti-S bond formed is stronger. These results confirm that the alkaline K_2S system can etch Ti and Al atoms in Mo_2TiAlC_2.

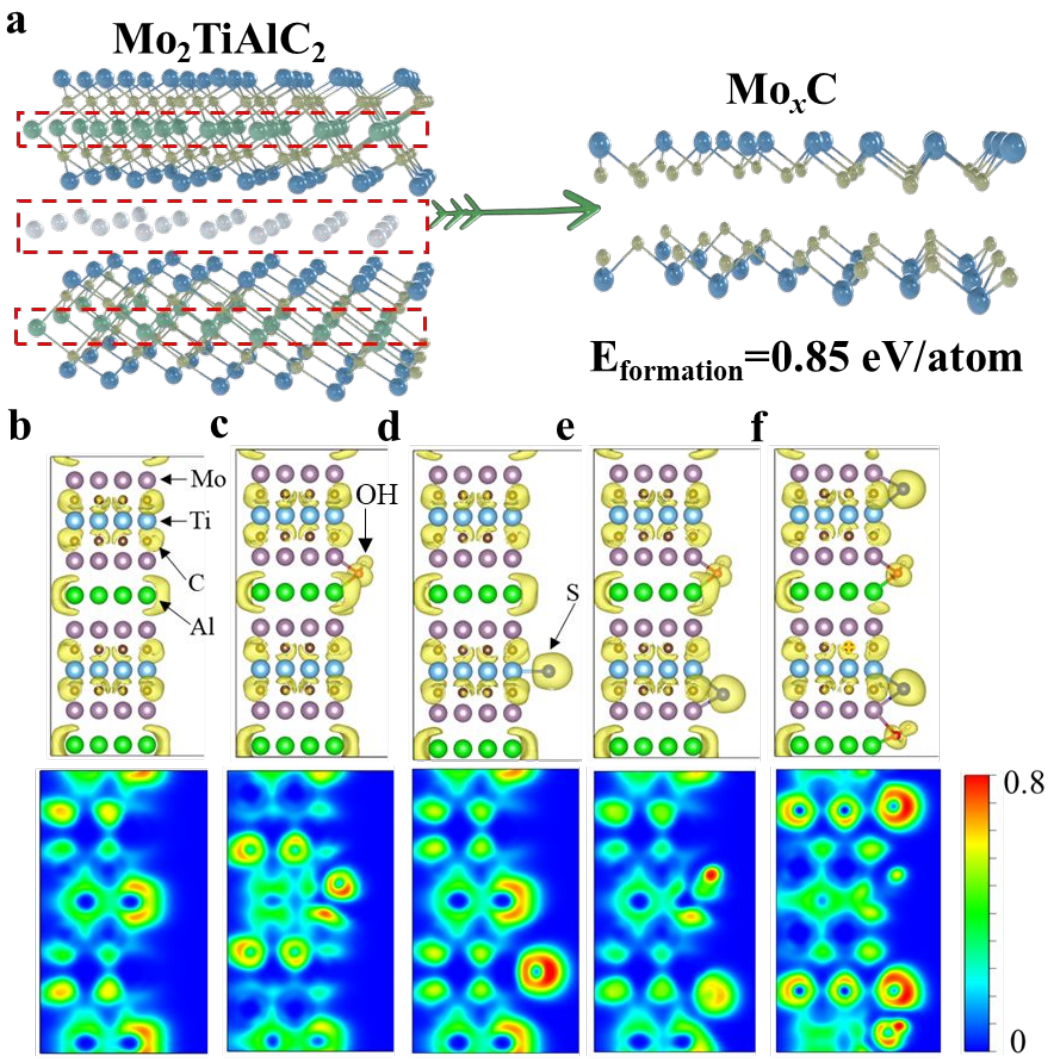

Figure 4. (a) The formation energies of Mo_xC by using the energy of Mo_2TiAlC_2 as the baseline. (Mo atoms: blue; Ti atoms: cyan; Al atoms: silve; C atoms: yellow). (b-f) Lowest-energy atomic configurations and their corresponding ELF plots of pristine Mo_2TiAlC_2 and etched Mo_2TiAlC_2 with increasing amounts of OH^- and S^{2-}.

X-ray photoelectron spectroscopy (XPS) was employed to identify surface metallic elements and their valence states. To compare the etched Mo_xC in solution with that deposited cathode, we analyzed their valence states at 3 V etching potential. In contrast to the elemental composition of the powder collected from the etching solution without KOH solution cleaning, XPS survey spectra of Mo_xC@CC do not detect the presence of titanium (Ti) and aluminum (Al) elements (Figure 5a). This observation implies that a substantial reduction of Ti and Al, indicating nearly complete etching of these elements. For Mo 3d spectrum (Figure 5b), the significant decrease in the peak intensity for

Mo_xC@CC confirms partial etching of the Mo atomic layer. The residual Mo atoms are found to be coordinated with Mo-C and Mo-O bonds. High-resolution XPS spectra of Ti and Al (Figure 5c, d) illustrate the presence of a large number of oxides in the etching solution, suggesting that electrochemical oxidation occurred at the anode, confirming the complete extraction of Ti and Al from Mo_2TiAlC_2. The high-resolution C 1s spectrum (Figure 5e) can be deconvoluted into peaks corresponding to C-Mo, C-C, C-OH, and C=O bonds.[36, 37]. Further analysis of the S 2p spectrum (Figure 5f) reveals the presence of the S_8 phase in the solution without KOH solution washing, being consistent with the XRD findings as mentioned previously. Moreover, the difference in the S XPS spectra between the solution and Mo_xC@CC shows that poorly conductive S_8 does not deposit on the carbon cloth cathode. The peak position (168.5 eV and 169.6 eV) coincides with unbonded SO_x.[34, 38, 39] The sulfur-containing species detected in our Mo_xC@CC electrodes are oxidized SO_x species (intercalation effect) introduced from the potassium sulfide (K_2S) electrolyte during the electrochemical etching process. Considering the literature reports on SO_x insertion during electrochemical exfoliation[38], we suggest that the inserted SO_x species might modify the surface electronic states and hydrophilicity of the catalyst, which could enhance electrolyte accessibility and facilitate electron transfer, thus impacting catalytic activity.

Our etching method using K_2S as the etching agent differs fundamentally from conventional HF-based approaches in several key aspects. Most notably, the use of K_2S eliminates the need for direct handling of hazardous hydrofluoric acid, significantly enhancing the safety and environmental compatibility of the process. Moreover, our method enables the synthesis of Mo_xC with a considerably shorter etching time and at a lower temperature compared to traditional acid-based methods. For instance, while most reported Mo-based MXene syntheses typically require approximately 72 hours of etching (Table S2), our K_2S-based electrochemical approach markedly reduces the processing time, thereby improving overall efficiency.

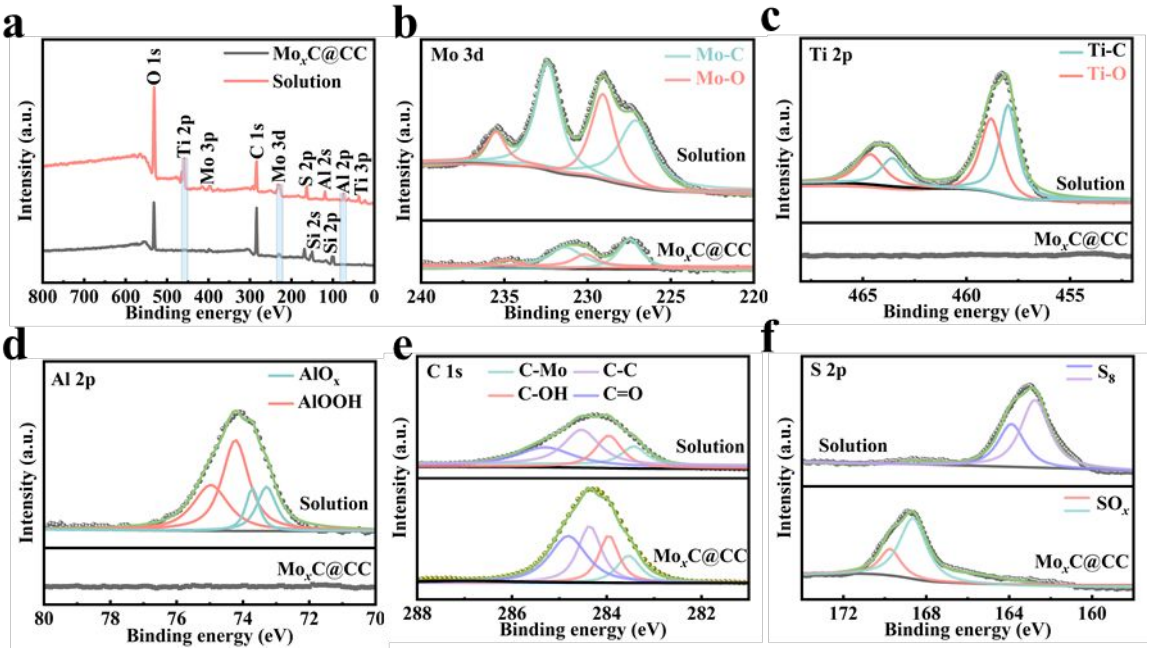

Figure 5. (a) Survey spectrum of Mo_xC powder in the solution without KOH solution cleaning and Mo_xC@CC at 3 V etching potential. (b) Mo 3d, (c) Ti 2p, (d) Al 2p, (e) C 1s, and (f) S 2p spectra of Mo_xC powder in the solution and Mo_xC@CC.

As a proof-of-concept demonstration, the HER activity of Mo_xC@CC catalysts (Figure 6) was evaluated in 0.5 M H_2SO_4 solution using a graphite rod as the counter electrode. The cathode-deposited Mo_xC@CC can be used directly as a test electrode, eliminating the need for the conventional preparation of the ink electrode for HER testing. The electrocatalytic activities of Mo_xC@CC were investigated for the samples prepared at different etching voltages ranging from 3 V to 5 V. For better normalization and comparison, three different mass loads (0.5, 1.2, and 3.8 mg cm^{-2}) were tested by adjusting the etching time at each potential (3, 4, and 5 V). The HER performances of the bare CC and the original Mo_2TiAlC_2 (Figure S8) were disappointing due to their bulky microstructural features, which lack active catalytic sites. For reference, commercial Pt/C exhibited superior electrocatalytic performance, achieving an overpotential of 56 mV at a current density of 10 mA cm^{-2} (Figure 6a). At an etching voltage of 3 V, the Mo_xC@CC with a mass load of 1.2 mg cm^{-2} exhibited an overpotential of 168 mV at a current density of 10 mA cm^{-2}, outperforming Mo_2TiAlC_2. Varying the mass load to 3.8 and 0.5 mg cm^{-2} resulted in overpotentials of 185 mV and 172 mV, respectively. Similarly, the optimal

HER overpotential can be achieved under the same mass load of 1.2 mg cm^{-2} for etching voltages of 4 V (Figure 6b) and 5 V (Figure 6c). Notably, all the Mo_xC@CC samples showed excellent performance among the non-precious metal catalysts even without iR correction. The enhanced catalytic activity of Mo_xC@CC can be attributed to the increase of the active site density caused by the electrochemical etching process and the presence of defects caused by the removal of metal atoms. The catalysts with different voltages and different mass loads exhibited obvious HER activity, with overpotentials remaining relatively consistent.

The Tafel slope is a crucial in electrochemistry for identifying rate-controlling steps and understanding the electron transfer kinetics of HER. At a 3 V etching voltage, the Mo_xC@CC catalysts with a 0.5 mg cm^{-2} mass load exhibited the lowest Tafel slope (92.28 mV dec^{-1}), indicating the fastest HER kinetics compared to 1.2 mg cm^{-2} (100.21 mV dec^{-1}) and 3.8 mg cm^{-2} (104.78 mV dec^{-1}) at 3 V voltage (Figure 6d). For the samples etched at 4 V (Figure 6e), the Tafel slopes were 102.80, 103.97, and 105.84 mV dec^{-1}. Tafel slopes ranging from 40 to 120 mV dec^{-1} suggest that the rate-determining step of HER is the desorption step of adsorbed hydrogen atom (H_{ad}).[40] For the samples etched at 5 V (Figure 6f), the Tafel slopes exceeded 120 mV dec^{-1}, suggesting that these catalysts follow the Volmer reaction mechanism, where the formation of H_{ad} on the active sites during the discharge step plays a crucial role. The intrinsic activity of the catalyst was further assessed using electrochemical double layer capacitance (C_{dl}) measurement. To analyze the C_{dl}, cyclic voltammetry (Figure S9) was performed across scan rates from 10 to 100 mV s^{-1}. As shown in Figure 6g, the calculated C_{dl} values for the 3 V-etched samples are successively 15.44, 39.04, and 44.49 mF cm^{-2} as the mass increases. This implied that the electrochemically active surface area of the Mo_xC@CC improved with higher mass loading. Similar trends were observed for the catalysts etched at 4 V and 5 V (Figure 6h-i). Electrochemical impedance spectroscopy (EIS) was used to determine the charge transfer resistance (R_{ct}) of the electrodes (Figure 6j-l), modeled using an equivalent circuit model (Figure S10). The R_{ct} values of Mo_xC@CC etched at 3 V were 51.12, 19.65, 14.66 Ω for three different loads of samples. The catalyst synthesized by etching at 4V exhibited

the lowest R_{ct} of 7.43 Ω, while the sample prepared at 5 V had the lowest R_{ct} value of 8.43 Ω, respectively. These low R_{ct} values for the Mo_xC@CC suggested good conductivity and thereby fast charge-transfer behavior, which contribute to enhanced HER kinetics.[10, 40] All the values obtained from the electrochemical experiments for all the Mo_xC@CC electrocatalysts are summarized in Table 1, highlighting their promising potential for non-precious metal-based HER catalysts[21, 29, 41-59] (Table 2).

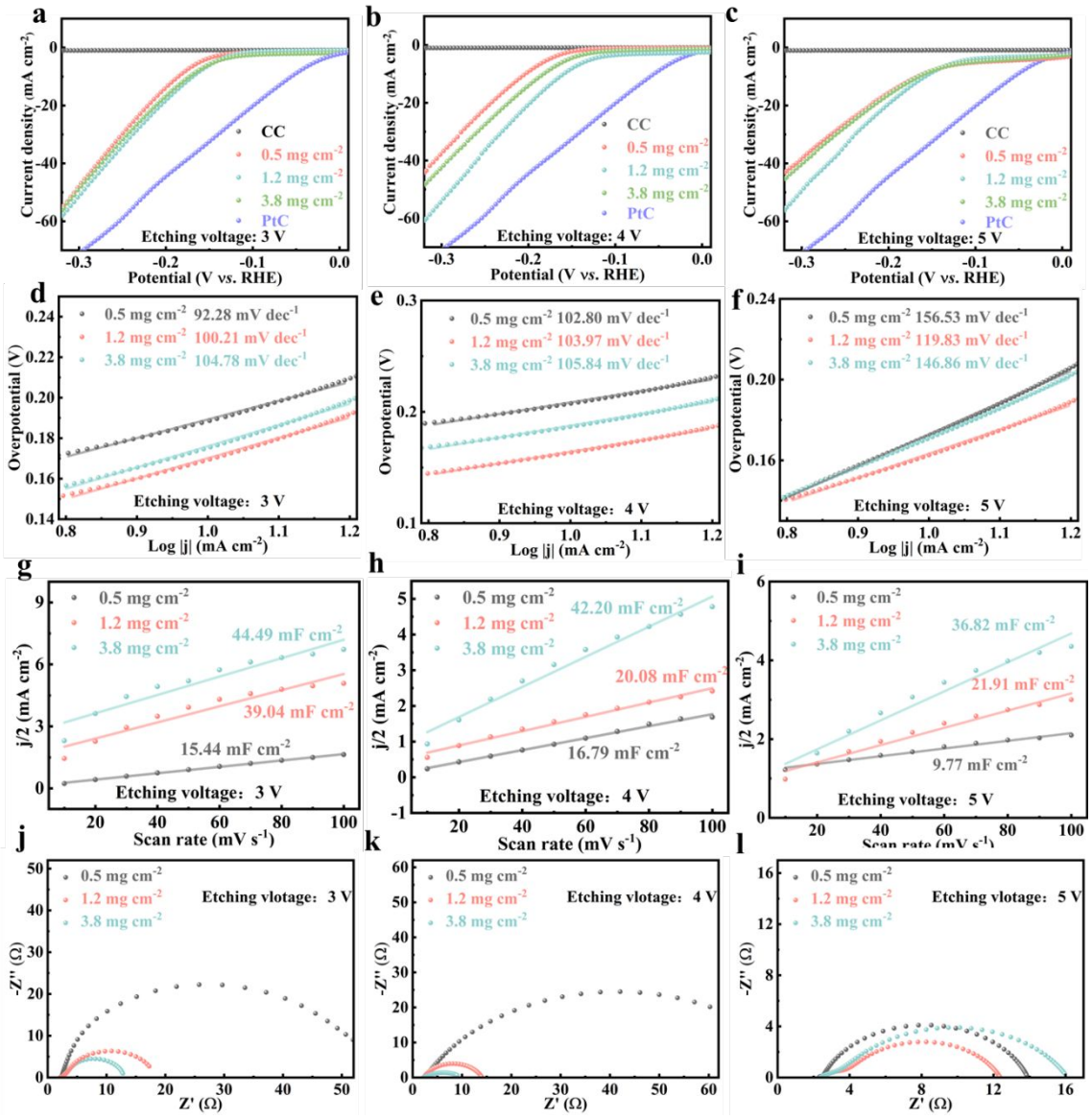

Figure 6. Linear scan curves of Mo_xC@CC under the etching voltage of (a) 3 V, (b) 4 V, and (c) 5 V at scanning rate of 5 mV s^{-1} in 0.5 M H_2SO_4. Corresponding Tafel plots of (d) 3 V, (e) 4 V, and (f) 5 V. Double-layer capacitance (C_{dl}) of (g) 3 V, (h) 4 V, and (i) 5 V. Nyquist plots of (j) 3 V, (k) 4 V, and (l) 5 V.

Assessing the long-term stability of HER catalyst is crucial for their practical applications. We performed time-current measurements at a fixed potential and examined variations in the LSV curve before and after durability testing. As depicted in Figure 7a, the original Mo_xC@CC generally exhibited excellent stability over a period of 24 hours, with the current density fluctuating around 10 mA cm^{-2} due to the bubble formation during HER. This is further supported by the negligible deviation observed between the LSV curves before and after HER (Figure 7b). Most importantly, XPS analysis after durability testing (Figure 7c) reveals no significant peak shifts or the emergence of new peaks observed in the Mo 3d spectrum (Figure 7d), indicating that the Mo_xC@CC sample remains highly stable under long-term HER conditions. In addition, SEM characterization (Figure 7e) confirms that the catalyst remained well-adhered to the carbon cloth substrate, maintaining its original morphology despite some small surface cracks. TEM image (Figure 7f) further demonstrates that the Mo_xC@CC structure remained amorphous with slightly enlarged pores. The HER cycle performance under high current density conditions is also important for practical applications. Figure 7g shows the current-time stability curve at potential of -0.3 V vs. RHE. After 14 h of operation (Figure 7h), the current density decays from the initial 50 mA cm^{-2} to 40 mA cm^{-2}. SEM image (Figure 7i) confirms that the H^+ intercalation effect of Mo_xC@CC under high current density leads to further stripping of Mo_xC, resulting in the partial active material falling off from the CC substrate. The significantly reduced Mo signal XPS characterization (Figure S11) also supports this view. Then, the overpotential change at 10 mA cm^{-2} is not obvious. The above stability results confirm the long-term stability of Mo_xC@CC at low current density and can maintain a certain activity at high current density. In order to demonstrate its actual operation of water electrolysis, we selected commercial RuO_2 as the OER catalyst and assembled it with Mo_xC@CC for water electrolysis experiments. As shown in Figure S12, 1.8 V can drive a current density of 50 mA cm^{-2}, and the actual operation photos are also provided in Figure S18a. As summarized in Table 2, the low overpotential and Tafel slope of Mo_xC@CC outperform those of other reported catalysts[21, 29, 41-59], highlighting its remarkable electrochemical performance. In addition, compared with the traditional HF acid chemical etching synthesis method (Table S2), our proposed electrochemical

etching method shows great advantages in the synthesis process, especially in terms of etching efficiency and environmental friendliness.

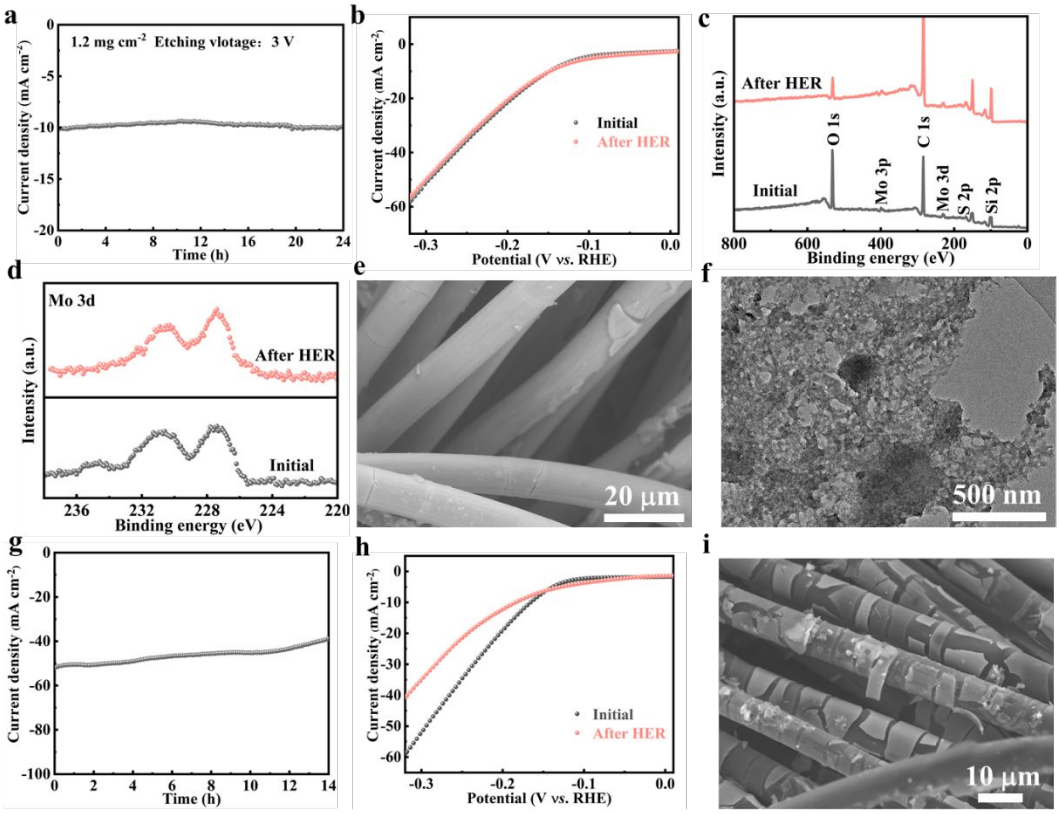

Figure 7. (a) Time dependence of the current density curve for 1.2 mg cm^{-2} Mo_xC@CC 3 V at an overpotential of 168 mV versus RHE. (b) LSV polarization curves of 1.2 mg cm^{-2} Mo_xC@CC 3 V before and after 24 h HER continuous operation. (c) XPS survey spectrum and (d) high-resolution XPS spectra of Mo 3d before and after HER operation. (e) SEM and (f) TEM image of 1.2 mg cm^{-2} Mo_xC@CC 3 V after 24 h HER continuous operation. (g) Time dependence of the current density curve for 1.2 mg cm^{-2} Mo_xC@CC 3 V at an overpotential of 300 mV vs. RHE. (h) LSV polarization curves of 1.2 mg cm^{-2} Mo_xC@CC 3 V before and after HER (300 mV vs. RHE) operation. (i) SEM image of after HER operation.

To further elucidate the catalytic mechanism, density functional theory (DFT) calculations were employed. Optimized models of the original Mo_2TiAlC_2 and the etched Mo_xC are shown in Figure 8a-d. The Gibbs free energy (ΔG_{H*}) of adsorbed hydrogen serves as a key indicator of HER catalytic activity. An ideal HER catalyst should have a

ΔG_{H^*} value close to zero. Figure 8e shows that Mo_2TiAlC_2 has a relatively negative ΔG_{H^*} value (−0.76 eV), indicating strong hydrogen adsorption, which leads to a thermodynamic barrier for H_2 desorption. Compared to the unetched Mo_2TiAlC_2, the ΔG_{H^*} value (-0.47 eV) of Mo_xC is reduced by 0.29 eV, suggesting faster hydrogen adsorption and desorption kinetics compared to Mo_2TiAlC_2. Furthermore, the density of states (DOS) plot (Figure 8f) reveals that the Mo_xC phase exhibits a significantly higher density of states near the Fermi level compared to Mo_2TiAlC_2. This increase in DOS near the Fermi level for Mo_xC suggests enhanced electron availability, contributing to improved conductivity and accelerated charge transfer during the HER process.

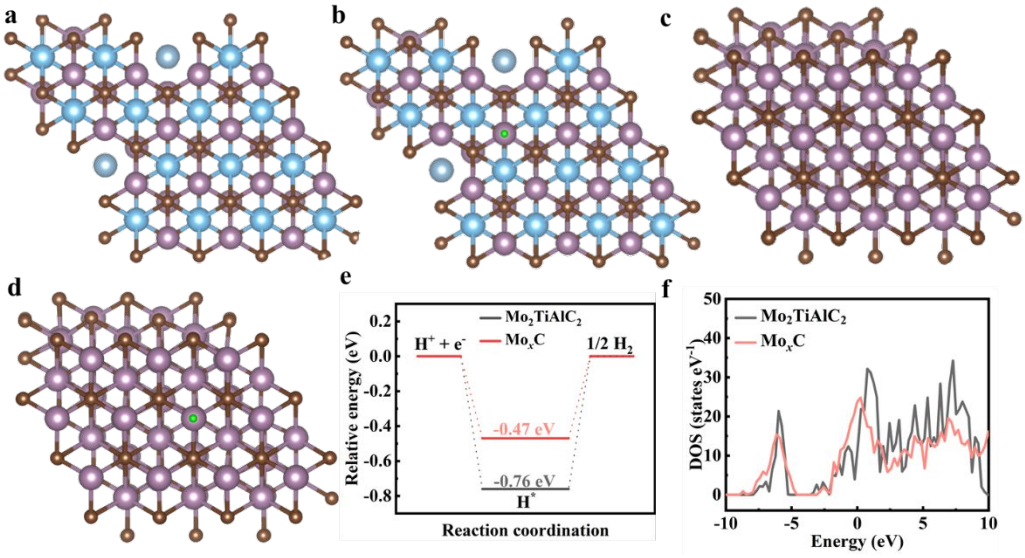

Figure 8. (a) Mo_2TiAlC_2 and (b) Mo_xC. The adopted adsorption sites of H* on the surface of the (c) Mo_2TiAlC_2 and (d) Mo_xC. Atoms in purple, blue, brown, silver, and green represent Mo, Ti, C, Al, and H, respectively. (e) Calculated ΔG_{H^*} and (f) corresponding DOS (the energy refers to the Fermi level) of the Mo_2TiAlC_2 and Mo_xC model catalysts.

Based on the abundant active sites and excellent conductivity of Mo_xC@CC, the electrochemical capacitive performance was further evaluated. Since the optimal HER performance was achieved at an etching voltage of 5 V, the capacitive performance was evaluated for varying mass loadings under this condition. As shown in Figure 9a-c, CVs were recorded at scan rates ranging from 2 mV s^{-1} to 200 mV s^{-1} within a potential range of -0.35 to 0.25V vs. SCE in 0.5 M H_2SO_4. The CV curve of Mo_xC@CC with a mass loading of 1.2 mg cm^{-2} (Figure 9d) encompasses a larger area compared to the others,

indicating it has the highest specific capacity. At a scan rate of 2 mV s^{-1}, the Mo_xC@CC with a mass loading of 1.2 mg cm^{-2} (Figure 9e) exhibited a specific capacitance of 394 F g^{-1}, significantly outperforming the samples with a mass loading of 0.5 mg cm^{-2} (194 F g^{-1}) and 3.8 mg cm^{-2} (100 F g^{-1}). As depicted in Figure 9f-h, the galvanostatic charge/discharge (GCD) curves recorded at varying current densities (1, 2, 3, 4, 5, and 10 A $g^{-1)}$ displayed nearly triangular and symmetric charge–discharge profiles, demonstrating highly reversible redox reactions during the charge–discharge cycles. At a current density of 1 A g^{-1}, the galvanostatic charge/discharge (GCD) curves of Mo_xC@CC with a mass loading of 1.2 mg cm^{-2} exhibitd the longest discharge duration among all the samples, aligning well with the CV results. Electrochemical impedance spectroscopy (EIS) was employed to gain deeper insight into electrochemical kinetics and charge transfer processes. As shown in Figure S13(a-b), the Nyquist plots exhibit a semicircle in the high-frequency region and a quasi-vertical line in the low-frequency region. Based on the fitting results of the equivalent circuit (Figure S13c), the charge transfer resistance (R_{ct}) values for the Mo_xC@CC (0.5, 1.2, 3.8 mg cm^{-2}) are 0.63 Ω, 1.13 Ω, and 1.24 Ω, respectively. Besides, after repeating the GCD test for 5000 cycles (Figure 9i) at a high current density of 10 A g^{-1}, Mo_xC@CC with a mass loading of 1.2 mg cm^{-2} sample retained 94.7% of its initial capacitance, demonstrating excellent cycling stability. Compared to the capacitive performance of currently reported carbides[32, 60-70] (Table 3), Mo_xC@CC demonstrates superior capacitance performance, making it a promising candidate for advanced energy storage applications.

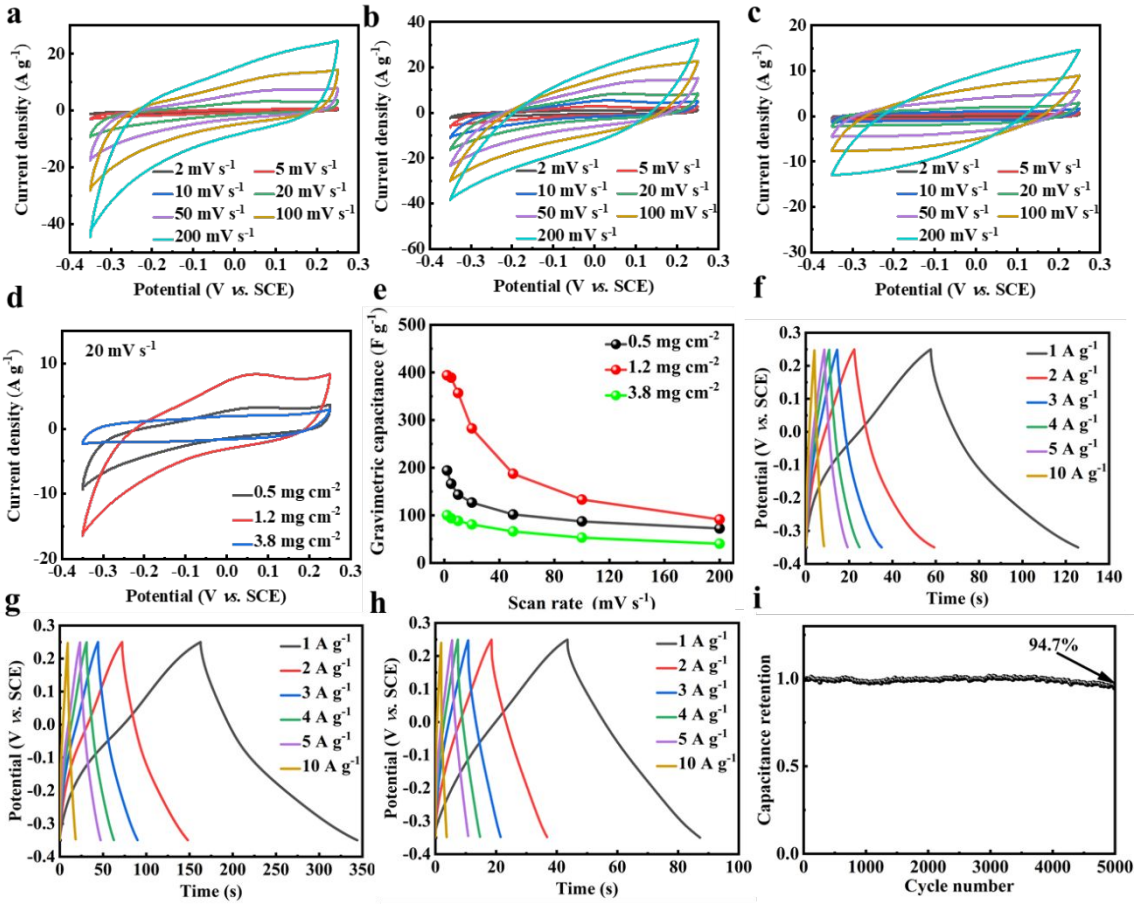

Figure 9. CV curves of Mo_xC@CC 5 V for (a) 0.5, (b) 1.2, and (c) 3.8 mg cm^{-2} mass loading electrodes at different scan rate. (d) CV curves of three Mo_xC@CC 5 V samples at scan rate of 20 mV s^{-1}. (e) Rate performances for three samples. GCD curves of (f) 0.5, (g) 1.2, and (h) 3.8 mg cm^{-2} mass loading. (i) Cycling performance curves of 1.2 mg cm^{-2}.

To further elucidate the energy storage mechanism of the Mo_xC@CC electrode, the electrochemical kinetic analysis was conducted. Specifically, the fitting parameter (*b*-value) was determined using electrochemical kinetic equations[16].

$$i = i_{cap} + i_{diff} = av^b \quad (1)$$

$$\log i = \log a + b \log v \quad (2)$$

where the i was measured in the CV test at different scan rates (v, mV s^{-1}) from 2 mV s^{-1} to 200 mV s^{-1}. The current (i) consists of two parts, including the diffusion-controlled process (i_{diff}) and the surface capacitance dominated process (i_{cap}).

As illustrated in Figure S14a, the linear fitting results show b values were 0.74 and 0.73

for the anodic and cathodic currents, respectively, indicating that the energy storage mechanism of Mo_xC@CC involves a typical mixed-controlled process, encompassing both diffusion-controlled and capacitive-controlled behaviors. The capacitive-controlled contributions (Figure S14b) at different scan rates from CV testing are illustrated, showing a significant increase from 12.4% at 2 mV s^{-1} to 52.9% at 200 mV s^{-1}. Furthermore, evaluating the real device performance is crucial for practical application of the supercapacitor. We have fabricated both symmetric and asymmetric (activated carbon (AC) as positive electrode) supercapacitor devices based on our electrode materials. Figure 10a-b shows the CV curves of symmetry Mo_xC@CC//Mo_xC@CC and asymmetry Mo_xC@CC//AC supercapacitors. The potential window for the symmetric device is only 0.5 V, while the potential window for asymmetry device can be extended to 1 V. Moreover, as observed in Figure 10c-d, the discharge time in the GCD curve for the asymmetric device are significantly greater than those of the symmetrical device. According to the Ragone plots (Figure 10e), the asymmetric device can obtain the maximum energy density of 12.4 Wh kg^{-1} at a power density of 89.1 W kg^{-1}. However, the symmetrical device can only obtain a maximum energy density of 1.7 Wh kg^{-1} at a power density of 24.6 W kg^{-1}. Also, the capacitance retention of 69.8% for symmetric device can be obtained after 1000 cycles at 1 A g^{-1} current density (Figure S15a). The SEM (Figure S15b) and TEM (Figure S15c) characterization confirms that the layered structure Mo_xC transforms into the band-shaped MoO_x. Raman spectroscopy (Figure S15d) also confirmed the vibration peak of MoO_x.[71] The cycle performance (Figure 10f) of Mo_xC@CC//AC is significantly better than that of symmetric supercapacitors, and the capacity retention rate (1 A g^{-1}) was still maintained at 80.2% after 6000 cycles of actual operation (Figure 10f). At a high current density of 5 A g^{-1}, the capacity retention rate (Figure S17a) was maintained at 78.5% after 3000 cycles. After cycling, the lamellar structure of the sample showed a certain degree of fragmentation and pulverization (Figure S16a, 17b). XPS test (Figure S16b, 17c) shows that the Mo 3d binding energy shifts significantly, indicating that the Mo element was partially oxidized to a high valence state (+5/+6). The two asymmetric supercapacitor devices in series lighted up red LED (Figure S18b). The electrochemical performance for Mo_xC@CC//AC is better than

those of most other supercapacitors, especially the energy density, as presented in Table S4.

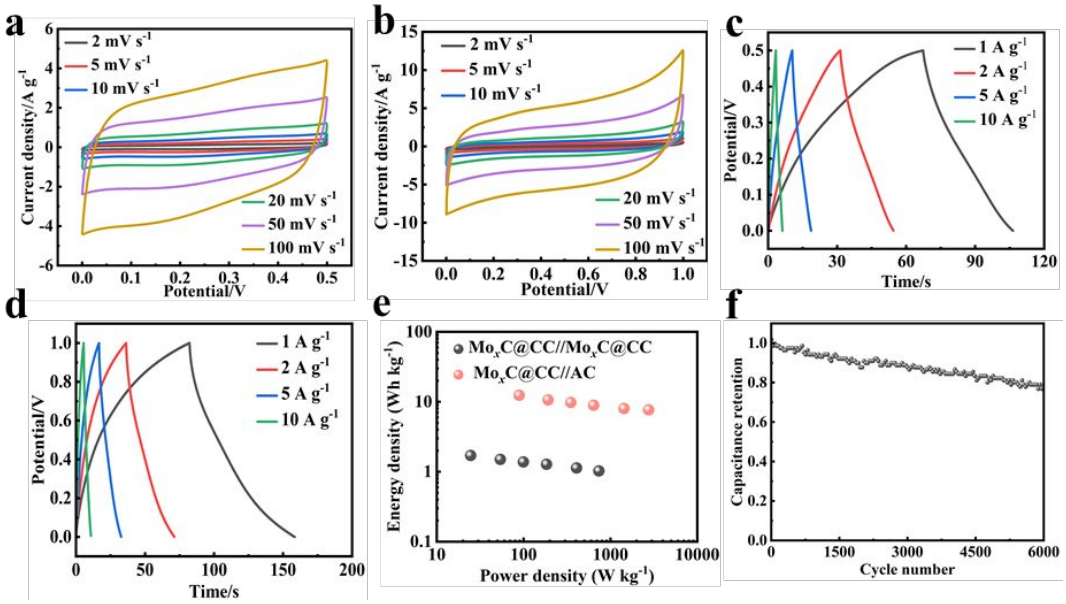

Figure 10. CV curves of (a) Mo_xC@CC//Mo_xC@CC symmetrical device. (b) Mo_xC@CC//AC asymmetric device at different scan rates in 0.5 M H_2SO_4. GCD curves of (c) symmetrical and (d) asymmetric device. (e) The Ragone plots of symmetrical and asymmetric device. (f) Cycling performance curves of asymmetric devices (1 A g^{-1}).

Table 1 Summary of HER performance of the as-fabricated Mo_xC@CC in 0.5 M H_2SO_4.

Samples	Mass loading (mg cm^{-2})	η_{10} (mV)	Tafel slope (mV dec^{-1})	C_{dl} (mF cm^{-2})	R_{ct} (Ω)
Mo_xC@CC 3 V	0.5	172	92.28	15.44	51.12
Mo_xC@CC 3 V	1.2	168	100.21	39.04	19.65
Mo_xC@CC 3 V	3.8	185	104.78	44.39	14.66
Mo_xC@CC 4 V	0.5	203	102.80	16.79	77.69
Mo_xC@CC 4 V	1.2	159	103.97	20.08	17.00
Mo_xC@CC 4 V	3.8	182	105.84	42.20	7.43
Mo_xC@CC 5 V	0.5	165	156.63	9.77	11.41

Mo_xC@CC 5 V	1.2	157	119.83	21.91	8.43
Mo_xC@CC 5 V	3.8	164	146.86	36.82	12.43

1 **Table 2** Summary of HER performance with previously studied materials.

Catalyst	Electrolyte	η_{10} (mV)	Tafel slope (mV dec^{-1})	Ref.
E-MXene	0.5 M H_2SO_4	225	93	[21]
$Ti_3C_2T_x$	0.5 M H_2SO_4	843	340	[41]
P−Mo_2CT_x,	0.5 M H_2SO_4	186	--	[42]
Ti_2CT_x	0.5 M H_2SO_4	609	124	[43]
Nb_2CT_x	0.5 M H_2SO_4	> 300	239	[44]
L-Mo_2C	0.5 M H_2SO_4	170	77	[45]
$Nb_4C_3T_x$	0.5 M H_2SO_4	398	122.2	[46]
MoS_x@Mo_2C	0.5 M H_2SO_4	--	44	[29]
Mo_2CT_x	0.5 M H_2SO_4	283	82	[43]
P-Mo_2C/Ti_3C_2@NC	0.5 M H_2SO_4	177	57.3	[47]
$V_4C_3T_x$	0.5 M H_2SO_4	~800	236	[48]
mNC-MoC/Ti_3C_2	0.5 M H_2SO_4	150	70.9	[49]
V_2CT_x	0.5 M H_2SO_4	760	187	[50]
Co_2P	0.5 M H_2SO_4	178	52	[51]
$CuWO_4$@rGO	0.5 M H_2SO_4	565	--	[52]
MoS_2/Co_xS_y	0.5 M H_2SO_4	135	71	[53]
CoTPP–PZSNT	0.5 M H_2SO_4	109	95	[54]
Ni_2P/CoP	0.5 M H_2SO_4	160	57	[55]
Ti_3C_2 NFs	0.5 M H_2SO_4	169	97	[56]
$Mo_2TiC_2T_x$	0.5 M H_2SO_4	248	74	[57]
$Mo_2Ti_2C_3T_x$	0.5 M H_2SO_4	275	99	[57]
$Mo_{1.33}C$	0.1 M $HClO_4$	422	--	[58]

$W_{1.33}C$	0.1 M $HClO_4$	320	--	[59]

Table 3. Comparison of measured electrochemical capacitance with previously studied materials.

Electrodes	Electrolyte	Potential window	Specific capacitance	Ref.
Mo_xC@CC 5 V	0.5 M H_2SO_4	-0.35 ~ 0.25V vs. SCE	394 F g^{-1} at 2 mV s^{-1}	This work
$V_4C_3T_x$	1.0 M H_2SO_4	-0.4 ~ 0.4V vs. Ag/AgCl	298 F g^{-1} at 2 mV s^{-1}	[60]
$Mo_{1.7}TiNb_{0.3}C_2T_x$,	3.0 M H_2SO_4	−0.8 ~ −0.1 V vs. Hg/Hg_2SO_4	398 F cm^{-3} at 2 mV s^{-1}	[32]
$Mo_{1.33}Nb_2C_3$	1.0 M H_2SO_4	-0.2 ~ 0.2V vs. Ag/AgCl	114.9 F g^{-1} at 2 mV s^{-1}	[61]
Li-V_2C	5.0 M LiCl	−1.2 ~ 0 V vs. Ag wire	155 F g^{-1} 2 mV s^{-1}	[62]
$Ti_3C_2T_x$	3.0 M H_2SO_4	-0.7 ~ 0.3V vs. Ag/AgCl	340.9 F g^{-1} at 2 mV s^{-1}	[63]
$Nb_4C_3T_x$	1.0 M H_2SO_4	−0.9 ~ 1 V vs. Ag	1075 F cm^{-3} at 5 mV s^{-1}	[64]
$Ti_3C_2T_x$	1.0 M Li_2SO_4	−0.8 ~ 0.0 V vs. Ag/AgCl	118 F g^{-1} at 1 A g^{-1}	[65]
WO_3–V_2O_5	1.0 M H_2SO_4	−0.8 ~ −0.2 V vs. Hg/Hg_2SO_4	246 F/g at 1 A g^{-1}	[66]
TpOMe-DAQ	3.0 M H_2SO_4	−0.5 ~ 0.5 V vs. Hg/Hg_2SO_4	169 F g^{-1} at 1 A g^{-1}	[67]
NSGO	1.0 M H_2SO_4	−0.1 ~ 0.7 V vs. Ag/AgCl	373 F g^{-1} at 0.5 A g^{-1}	[68]
Porous carbon	1.0 M H_2SO_4	-0.4 ~ 0.6 V vs. SCE	389 F g^{-1} at 0.2 A g^{-1}	[69]
rGO	1.0 M H_2SO_4	0 ~ 0.9 V vs. Ag/AgCl	164.6 F g^{-1} at 1 A g^{-1}	[70]

3. Conclusion

This study presents a novel electrochemical etching method for synthesizing molybdenum carbide (Mo_xC) materials with exceptional catalytic performance for hydrogen evolution reaction and high specific capacitance. Through a comprehensive investigation involving both experimental approaches and density functional theory (DFT) calculations, the etching mechanism from the quaternary carbide (Mo_2TiAlC_2) precursor to Mo_xC was elucidated. The results demonstrate that Ti and Al atoms, along with a portion of Mo, can be entirely removed *via* electrochemical etching in an alkaline K_2S

solution, producing Mo_xC nanosheets with abundant metal vacancy defects. The nanosheets exhibit remarkable HER catalytic activity, delivering ultralow overpotentials (157 mV at 10 mA cm^{-2}) in 0.5 M H_2SO_4. Theoretical calculations reveal that Mo_xC possesses a reduced Gibbs free energy change for HER, indicating excellent catalytic performance. Also, Mo_xC@CC demonstrates as an excellent candidate for supercapacitor applications, exhibiting a high specific capacitance of 394 F g^{-1} at a scan rate of 2 mV s^{-1} and excellent cycling stability, retaining nearly 94.7% of its initial capacity after 5000 cycles. The as-fabricated asymmetric supercapacitor exhibits maximum energy density of 12.4 Wh kg^{-1} at a power density of 89.1 W kg^{-1} and the capacity retention rate was still up to 80.2% even after 6000 cycles at a current density of 1 A g^{-1}. This process is not only simple and efficient but also offers a promising new approach for synthesizing high-performance dual-functional active electrode materials.

Supporting Information

Supporting Information is available from the author.

Declaration of Competing Interest

The authors declare no conflict of interest.

Acknowledgments

This work was supported by Key Science and Technology Developing Project of Shaanxi Province (2020KWZ-004 to W.Q.), "Scientist + Engineer" Project of Shaanxi Province (2022KXJ-162 to W.Q.), China Postdoctoral Science Foundation (No. BX20200266, 2020M673400 to Y.Y.), and JST ERATO Yamauchi Materials Space-Tectonics Project (JPMJER2003). The XPS and TEM experiments were conducted at the Instrument Analysis Center, Xi'an Jiaotong University.

References

1 C. Yang, R. Zhao, H. Xiang, J. Wu, W. Zhong, X. Li and Q. Zhang, *Nano Energy*, 2022, **98**, 107232.

2 M. Yi, S. Hu, N. Li, H. Wang and J. Zhang, *J. Energy Chem.*, 2022, **72**, 453-464.

3 M. Sheng, Y. Yang, X. Bin and W. Que, *Materials*, 2023, **16**, 1529.

4 J. Lin, D. Yin, W. He, L. Wang, B. Yue, T. Wang, D. Li, C. Han and X. Dong, *Chem. Eng. J.*, 2024, **488**, 151195.

5 M. Sheng, Y. Yang, X. Bin, S. Zhao, C. Pan, F. Nawaz and W. Que, *Nano Energy*, 2021, **89**, 106468.

6 S. Hussain, I. Rabani, D. Vikraman, A. Feroze, M. Ali, Y.-S. Seo, W. Song, K.-S. An, H.-S. Kim, S.-H. Chun and J. Jung, *Chem. Eng. J.*, 2021, **421**, 127843.

7 M. Sheng, X. Bin, Y. Yang, Y. Tang and W. Que, *Mater. Lett.*, 2021, **311**, 131624.

8 S. Hussain, I. Rabani, D. Vikraman, A. Feroze, K. Karuppasamy, Z. u. Haq, Y.-S. Seo, S.-H. Chun, H.-S. Kim and J. Jung, *ACS Sustainable Chem. Eng.*, 2020, **8**, 12248-12259.

9 Z. N. Hu, Y. Ai, W. Xu, X. Zhang, Z. Sun, L. Guo, R. Guo, Y. Wang, K. Ding, H. B. Sun, J. Hu, Q. Liang and Y. Yang, *Small*, 2022, **18**, e2200439.

10 M. Liu, Y. Jiang, Z. Cao, L. Liu, H. Chen and S. Ye, *J. Energy Chem.*, 2024, **96**, 464-471.

11 R. Fang, H. He, Z. Wang, Y. C. Han and F. R. Fan, *Mater. Horiz.*, 2024, DOI: 10.1039/d4mh00225c.

12 J. Deng, P. Ren, D. Deng and X. Bao, *Angew. Chem. Int. Ed.*, 2015, **54**, 2100-2104.

13 J. Halim, S. Kota, M. R. Lukatskaya, M. Naguib, M.-Q. Zhao, E. J. Moon, J. Pitock, J. Nanda, S. J. May, Y. Gogotsi and M. W. Barsoum, *Adv. Funct. Mater.*, 2016, **26**, 3118-3127.

14 X. Bin, M. Sheng, B. Kong, Y. Luo, J. Xiao and W. Que, *Nanoscale*, 2024, **16**, 15196-15207.

15 X. Bin, M. Sheng, Y. Luo and W. Que, *Adv. Mater. Interfaces*, 2022, **9**, 2200231.

16 X. Bin, M. Sheng, Y. Luo and W. Que, *Electrochim. Acta*, 2023, **446**, 142070.

17 X. Bin, Y. Tian, Y. Luo, M. Sheng, Y. Luo, M. Ju and W. Que, *Electrochim. Acta*, 2021, **389**, 138774.

18 S. Y. Pang, Y. T. Wong, S. Yuan, Y. Liu, M. K. Tsang, Z. Yang, H. Huang, W. T. Wong and J. Hao, *J. Am. Chem. Soc.*, 2019, **141**, 9610-9616.

19 W. Sun, S. A. Shah, Y. Chen, Z. Tan, H. Gao, T. Habib, M. Radovic and M. J. Green, *J. Mater. Chem. A*, 2017, **5**, 21663-21668.

20 S.-Y. Pang, W.-F. Io, L.-W. Wong, J. Zhao and J. Hao, *Nano Energy*, 2022, **103**, 107835.

21 M. Sheng, X. Bin, Y. Yang, Z. Chen and W. Que, *Adv. Mater. Technol.*, 2023, **9**, 2301694.

22 S. Yang, P. Zhang, F. Wang, A. G. Ricciardulli, M. R. Lohe, P. W. M. Blom and X. Feng, *Angew. Chem. Int. Ed.*, 2018, **57**, 15491-15495.

23 M. Sheng, X. Bin, Y. Yang, Y. Tang and W. Que, *Small*, 2022, **18**, 2203471.

24 S. M. Varghese, S. R. Sarath Kumar and R. B. Rakhi, *Appl. Phys. Lett.*, 2024, **124**, 023905.

25 J. Wu, X. Zhang, Z. Li, C. Yang, W. Zhong, W. Li, C. Zhang, N. Yang, Q. Zhang and X. Li, *Adv. Funct. Mater.*, 2020, **30**, 2004348.

26 M. R. Lukatskaya, J. Halim, B. Dyatkin, M. Naguib, Y. S. Buranova, M. W. Barsoum and Y. Gogotsi, *Angew. Chem. Int. Ed.*, 2014, **53**, 4877-4880.

27 X. Yang, J. Cheng, X. Yang, Y. Xu, W. Sun and J. Zhou, *Chem. Eng. J.*, 2023, **451**, 138977.

28 T. Guo, H. Fei, R. Liu, F. Liu, D. Wang and Z. Wu, *Appl. Catal. B Environ.*, 2024, **343**, 123480.

29 C. Tang, W. Wang, A. Sun, C. Qi, D. Zhang, Z. Wu and D. Wang, *ACS Catal.*, 2015, **5**, 6956-6963.

30 S. Yuan, Y. Liu, J. Zheng, M. Cui, K. Wang and N. Li, *J. Alloys Compd.*, 2023, **933**, 167664.

31 J. Zhang, Y. Zhao, X. Guo, C. Chen, C. L. Dong, R. S. Liu, C. P. Han, Y. Li, Y. Gogotsi and G. Wang, *Nat. Catal.*, 2018, **1**, 985-992.

32 J. Zhao, W. Yan, Z. Liu, X. Liu, Y. Tian and X. Cui, *Nano Res.*, 2024, **17**, 7174–7181.

33 J. Chen, M. Chen, W. Zhou, X. Xu, B. Liu, W. Zhang and C. Wong, *ACS Nano*, 2022, **16**, 2461-2470.

34 F. Wang, F. Tian, X. Xia, Z. Pang, S. Wang, X. Yu, G. Li, Y. Zhao, Q. Xu, S. Hu, L. Ji, X. Zou and X. Lu, *Angew. Chem. Int. Ed.*, 2024, **63**, e202405315.

35 C. Wang, H. Shou, S. Chen, S. Wei, Y. Lin, P. Zhang, Z. Liu, K. Zhu, X. Guo, X. Wu, P. M. Ajayan and L. Song, *Adv. Mater.*, 2021, **33**, e2101015.

36 C. Zhang, C. Lu, S. Bi, Y. Hou, F. Zhang, M. Cai, Y. He, S. Paasch, X. Feng, E. Brunner and X. Zhuang, *Front. Chem. Sci. Eng.*, 2018, **12**, 346-357.

37 M. Q. Zhao, M. Sedran, Z. Ling, M. R. Lukatskaya, O. Mashtalir, M. Ghidiu, B. Dyatkin, D. J. Tallman, T. Djenizian, M. W. Barsoum and Y. Gogotsi, *Angew. Chem. Int. Ed.*, 2015, **54**, 4810-4814.

38 C. J. Raj, R. Manikandan, P. Thondaiman, P. Sivakumar, A. D. Savariraj, W.-J. Cho, B. C. Kim and H. Jung, *Carbon*, 2021, **184**, 266-276.

39 J. Landwehr, H. Steldinger and B. J. M. Etzold, *Catalysis Today*, 2018, **301**, 191-195.

40 K. M. M. D. K. Kimbulapitiya, B. Rehman, S. S. Wani, C.-T. Chen, R.-H. Cyu, A. Manikandan, M. K. Date, Y.-R. Peng, R. J. G. L. R. Kumara, F.-C. Chuang and Y.-L. Chueh, *Nano Energy*, 2024, **122**, 109235.

41 M. Bat-Erdene, M. Batmunkh, B. Sainbileg, M. Hayashi, A. S. R. Bati, J. Qin, H. Zhao, Y. L. Zhong and J. G. Shapter, *Small*, 2021, **17**, e2102218.

42 G. Qu, Y. Zhou, T. Wu, G. Zhao, F. Li, Y. Kang and C. Xu, *ACS Appl. Energy Mater.*, 2018, **1**, 7206-7212.

43 Z. W. Seh, K. D. Fredrickson, B. Anasori, J. Kibsgaard, A. L. Strickler, M. R. Lukatskaya, Y. Gogotsi, T. F. Jaramillo and A. Vojvodic, *ACS Energy Lett.*, 2016, **1**, 589-594.

44 X. Fan, P. Du, X. Ma, R. Wang, J. Ma, Y. Wang, D. Fan, Y. Long, B. Deng, K. Huang and H. Wu, *Materials*, 2021, **14**, 2426.

45 W. Yuan, Q. Huang, X. Yang, Z. Cui, S. Zhu, Z. Li, S. Du, N. Qiu and Y. Liang, *ACS Appl. Mater. Interfaces*, 2018, **10**, 40500–40508.

46 Y. Tan, Z. Zhu, X. Zhang, J. Zhang, Y. Zhou, H. Li, H. Qin, Y. Bo and Z. Pan, *Int. J. Hydrogen Energy*, 2021, **46**, 1955-1966.

47 Y. Tang, C. Yang, M. Sheng, X. Yin and W. Que, *ACS Sustainable Chem. Eng.*, 2020, **8**, 12990-12998.

48 M. H. Tran, T. Schäfer, A. Shahraei, M. Dürrschnabel, L. Molina-Luna, U. I. Kramm and C. S. Birkel, *ACS Appl. Energy Mater.*, 2018, **1**, 3908-3914.

49 Y. Tang, C. Yang, Y. Xie, Y. Kang, W. Que, J. Henzie and Y. Yamauchi, *ACS Sustainable Chem. Eng.*, 2022, **11**, 168-176.

50 Y. Yoon, A. P. Tiwari, M. Choi, T. G. Novak, W. Song, H. Chang, T. Zyung, S. S. Lee, S. Jeon and K. S. An, *Adv. Funct. Mater.*, 2019, **29**, 1903443.

51 B. T. Jebaslinhepzybai, T. Partheeban, D. S. Gavali, R. Thapa and M. Sasidharan, *Int. J. Hydrogen Energy*, 2021, **46**, 21924-21938.

52 J. Ahmed, N. Alhokbany, T. Ahamad and S. M. Alshehri, *New J. Chem.*, 2022, **46**, 1267-1272.

53 M. Zhang, W.-Z. Chen, Z.-L. Liu, J. He and Y.-Q. Wang, *Electrochim. Acta*, 2022, **433**, 141269.

54 X. Yang, W. Zhao, A. Wang, X. Zhai, Y. Dou, K. Syed and W. Zhu, *Chemical Communications*, 2024, **60**, 5594-5597.

55 Y. Xu, R. Wang, Y. Zheng, L. Zhang, T. Jiao, Q. Peng and Z. Liu, *Appl. Surf. Sci.*, 2020, **509**, 145383.

56 W. Yuan, L. Cheng, Y. An, H. Wu, N. Yao, X. Fan and X. Guo, *ACS Sustainable Chem. Eng.*,

2018, **6**, 8976-8982.

57 A. D. Handoko, K. D. Fredrickson, B. Anasori, K. W. Convey, L. R. Johnson, Y. Gogotsi, A. Vojvodic and Z. W. Seh, *ACS Appl. Energy Mater.*, 2017, **1**, 173-180.

58 S. Intikhab, V. Natu, J. Li, Y. Li, Q. Tao, J. Rosen, M. W. Barsoum and J. Snyder, *J. Catal.*, 2019, **371**, 325-332.

59 R. Meshkian, M. Dahlqvist, J. Lu, B. Wickman, J. Halim, J. Thornberg, Q. Tao, S. Li, S. Intikhab, J. Snyder, M. W. Barsoum, M. Yildizhan, J. Palisaitis, L. Hultman, P. O. A. Persson and J. Rosen, *Adv. Mater.*, 2018, **30**, 1706409.

60 Y. Wang, B. Zhou, Q. Tang, Y. Yang, B. Pu, J. Bai, J. Xu, Q. Feng, Y. Liu and W. Yang, *Adv. Mater.*, 2024, **36**, e2410736.

61 H. Guo, X. Fu, L. Peng, C. Wang, Y. Zhuang, H. Chong, Z. Chen, W. Gong, M. Yan, Q. Wang and W. Cui, *Adv. Mater.*, 2024, **36**, e2404466.

62 M. Saraf, T. Zhang, T. Averianov, C. E. Shuck, R. W. Lord, E. Pomerantseva and Y. Gogotsi, *Small Methods*, 2023, **7**, 2201551.

63 Z. Huang, J. Qin, Y. Zhu, K. He, H. Chen, H. Y. Hoh, M. Batmunkh, T. M. Benedetti, Q. Zhang, C. Su, S. Zhang and Y. L. Zhong, *Carbon Energy*, 2023, **5**, e295.

64 S. Zhao, C. Chen, X. Zhao, X. Chu, F. Du, G. Chen, Y. Gogotsi, Y. Gao and Y. Dall'Agnese, *Adv. Funct. Mater.*, 2020, **30**, 2000815.

65 T.-H. Chang, T. Zhang, H. Yang, K. Li, Y. Tian, J. Y. Lee and P.-Y. Chen, *ACS Nano*, 2018, **12**, 8048–8059.

66 P. Periasamy, T. Krishnakumar, M. Sandhiya, M. Sathish, M. Chavali, P. F. Siril and V. P. Devarajan, *Mater. Lett.*, 2019, **236**, 702-705.

67 A. Halder, M. Ghosh, M. A. Khayum, S. Bera, M. Addicoat, H. S. Sasmal, S. Karak, S. Kurungot and R. Banerjee, *J. Am. Chem. Soc.*, 2018, **140**, 10941-10945.

68 S. D, S. B. S, G. K. K R, V. V and P. A, *Electrochim. Acta*, 2024, **506**, 145007.

69 D. Tang, Y. Luo, W. Lei, Q. Xiang, W. Ren, W. Song, K. Chen and J. Sun, *Appl. Surf. Sci.*, 2018, **462**, 862-871.

70 N. Sykam, V. Madhavi and G. M. Rao, *J. Environ. Chem. Eng.*, 2018, **6**, 3223-3232.

71 Y. Sun, J. Wang, B. Zhao, R. Cai, R. Ran and Z. Shao, *J. Mater. Chem. A*, 2013, **1**, 4736-4746.

Data availability

Data supporting this study are included within the article and/or ESI.